IEEE Access
Multidisciplinary ⋮ Rapid Review ⋮ Open Access Journal

Received 26 November 2022, accepted 13 December 2022, date of publication 3 January 2023, date of current version 6 January 2023.

Digital Object Identifier 10.1109/ACCESS.2022.3233831

RESEARCH ARTICLE

Piecewise Weighted Smoothing Regularization in Tight Framelet Domain for Hyperspectral Image Restoration

FEI MA[1], SIYU LIU[1], FEIXIA YANG[2], AND GUANGXIAN XU[1]

[1]School of Electronic and Information Engineering, Liaoning Technical University, Huludao, Liaoning 125105, China
[2]School of Electrical and Control Engineering, Liaoning Technical University, Huludao, Liaoning 125105, China

Corresponding author: Siyu Liu (soyuliu729@gmail.com)

This work was supported in part by the Scientific Research Project of Colleges from Liaoning Department of Education (P. R. C.) under Grant LJKZ0357 and Grant LJ2020JCL012, in part by the National Key Research and Development Program of China under Grant 2018YFB1403303, and in part by the Discipline Innovation Team of Liaoning Technical University under Grant LNTU20TD-20 and Grant LNTU20TD-25.

ABSTRACT Hyperspectral images captured by remote-sensing satellites are easily corrupted by various types of noise. Generally, hyperspectral signatures appear to be scattered in spatial-spectral domain, as well as noise. In transform domain, however, the principal components of a image are often centralized in the low-frequency band, while noise and some details are mainly contained in high-frequency components. The traditional transformation domain based smoothing methods take no account of the respective information distribution carried by different frequency bands. Hyperspectral image restoration aims to remove mixed noise for clean data, which usually amounts to an ill-posed inverse problem. Moreover, the matrix-decomposition-based model needs to reshape hyperspectral datacube into matrix form, which will lead to certain loss of spatial structure information. In order to address these issues, this paper incorporates piecewise weighted smoothing regularization in tight framelet domain to reformulate a novel convex model for hyperspectal image restoration, which maintains image signature to a great extent. Based on the noise-perturbed degradation model, the smoothing regularizer in tight framelet domain is imposed on abundance signature, in which the transformation matrix, as well as the weighted coefficient, is well designed for different frequency bands. As a surrogate of sparsity, the l_q-norm is employed to denoise for the enhancement of hyperspectral signatures. To the end, an efficient solver is carefully designed to derive the closed-form solutions by proximal alternating optimization. The experimental results on several synthetic and real datasets, not only demonstrate that the performance of proposed method is better than that of the current state-of-the-art approaches, but also verify the validation of regularization terms for hyperspectral image restoration.

INDEX TERMS Hyperspectral image restoration, tight framelet domain, piecewise weighted smoothing, degradation model, mixed noise.

I. INTRODUCTION

Hyperspectral imagery is a data cube, which contains rich spatial geometric information and spectral signatures. It is widely used in environmental monitoring, material classification [1], target detection [2] and others [3]. However, in the course of data acquisition and processing, hyperspectral images (HSIs) are easily contaminated by different noise, such as Gaussian noise, salt and pepper noise and stripe noise [4]. This will seriously affect the quality and application of hyperspectral data [5], [6], [7]. Therefore, image restoration has become a hot topic to reconstruct high-fidelity hyperspectral data in remote sensing.

In recent years, there have been a large number of hyperspectral image restoration methods, which generally fall into three categories in terms of models, including

The associate editor coordinating the review of this manuscript and approving it for publication was Yi Zhang.

deep learning [8], tensor decomposition [9] and matrix factorization [10]. With the rapid development of artificial intelligence, deep learning based on unsupervised [11] or supervised [12] mechanism, is leveraged to reconstruct the super-resolution images, in which the unsupervised techniques don't need a large number of pure hyperspectral image datasets for training. For example, Sidorov et al. [13] developed a convolutional encoder-decoder network to implicitly induce a image prior in denoising. In the aspect of supervised methods, Xie et al. proposed a convolution neural network with trainable nonlinear functions for hyperspectral image restoration [14]. Zhuang et al. [15] adopted a fast and flexible denoising convolutional neural network to capture high local correlation in spatial subspace. However, deep learning based methods often involve a great deal of data training, as well as hyperparameters, which will lead to an increase in computational burden [16], [17]. Hyperspectral datacubes can be viewed as third-order tensors, so tensor decomposition and approximation are applicable for image restoration [18]. Recently, the widely-used tensor decomposition methods mainly include Tucker decomposition [19], tensor ring decomposition [20], BTD decomposition [21], Mode-3 decomposition [22] and so on. Ma et al. [23] incorporated graph smoothing and low-rank regularization into the model of Tucker tensor decomposition. Chen [24] constructed a low-rank tensor decomposition model to capture global spatial–spectral correlation. On the basis of low-rank Mode-3 decomposition, Zheng et al. [25] proposed a denoising method by introducing weighted group sparsity and total variation for spatial-spectral smoothing. Using low-rank approximation functions such as γ norm [26], weighted Schatten p-norm [27], [28] and tensor nuclear norm [29], the low-rank approximation of hyperspectral images can be realized. Specifically, Fan et al. [30] developed a low-rank hyperspectral image restoration model based on tensor singular value decomposition. The rank of a tensor, however, is not unique, which is different from that of a matrix. Furthermore, the tensor based methods also take much heavy computation. Another popular method is based on matrix factorization, in which hyperspectral cubic data needs to be reshaped into matrix form. Thus, the transformed two-dimensional hyperspectral data can be factorized into the product of endmember matrix and abundance signature, but the reconstruction is an ill-posed inverse problem that can be solved by the regularization method [31]. Zhang et al. [32] proposed a two-dimension HSI restoration method by establishing the framework of low-rank matrix restoration. Cao et al. brought forward a method by utilizing successive singular value decomposition to similar 3-D patches, based on low-rank matrix factorization [33]. Chen et al. [34] achieved spatial smoothness on the basis of low-rank nonnegative matrix factorization. In addition, total variation regularization is also an efficient method to explore the spatial-spectral local smoothness of HSI [35]. For example, Peng et al. [36] firstly introduced a enhanced 3-D total variation into HSI denoising model. Although spectral and abundance signatures have respective explicit physical meaning, reshaping hyperspectral datacube into matrix form will cause certain loss of structure information [37].

Generally, the image signatures are scattered in spatial-spectral domain, while they are centralized in transform domain. Furthermore, the principal components are often contained in the low-frequency bands while the details usually occur in the high-frequency parts [38]. The processing method in transform domain is then introduced into hyperspectral image restoration for better reconstruction performance [39]. For example, Zheng et al. [40] exploited the smoothness prior in third modes of the underlying tensor by introducing smoothness constraints to abundance matrix in transform domains and total variation regularizer to spectral library. Xu et al. [41] adopted the spatial-spectral joint weighting regularization on abundance matrix in the transform domains to promote the sparsity. The above transform-based smoothing method imposed same weight to the image in all frequency bands, which neglected the distribution characteristics of information signature in different frequency.

To address the above problems, this paper proposes a novel method by incorporating piecewise weighted smoothing regularization in tight framelet domain (PWSR-TF). The main contributions in this paper are described below. Firstly, using the noise-perturbed degradation model, the piecewise smoothing regularization is exerted on abundance matrix in tight framelet domain, and the weighted coefficient matrix is constructed to refine the information of different frequency bands. Secondly, l_q-norm regularization is used to promote the sparsity expression of sparse noise and framelet-based abundance matrix. Finally, an efficient solving algorithm is scrupulously designed by alternating optimization to obtain the closed-form solutions. In addition, the experimental tests demonstrate that the proposed PWSR-TF produces better performance than the state-of-the-art approaches for hyperspectral image restoration.

The remaining chapters of this paper are arranged as follows: Section II comes up with the noise-perturbed degradation model and the relevant regularization terms. Then, the detailed solution of the proposed algorithm is given in Section III. Nextly, Section IV is utilized to conduct the experimental test and performance analysis. Finally, the conclusion is drew in Section V. Besides these, some key notations are listed in the following sections. $\mathbb{R}$, $\mathbb{R}^n$ and $\mathbb{R}^{m\times n}$ denote the set of real number, n-vector and $m \times n$ matrices, respectively. $\|\cdot\|_1$ stands for l_1-norm. $\|\cdot\|_F$ denotes Frobenius norm. $\mathbf{I}$ stands for the identity matrix with proper dimensions. $\otimes$ represents the Kronecker product. $\odot$ denotes the dot product. $\succeq$ stands for the componentwise inequality operation.

II. SIGNAL MODELS AND REGULARIZATION TERMS

A. RESTORATION MODEL

HSIs are easily contaminated by noise in the process of acquisition and transmission. Assume that $\mathcal{Y} \in \mathbb{R}^{L_1\times L_2\times M}$ denotes the hyperspectral cubic data, where $L = L_1 \times L_1$

represents the number of spatial pixels, and M denotes the number of spectral bands. Using matrix factorization, the hyperspectral datacube $\mathcal{Y}$ can be reshaped as a matrix $\mathbf{Y} = [\mathbf{y}_1, \ldots, \mathbf{y}_i, \ldots, \mathbf{y}_L]$, where $\mathbf{y}_i \in \mathbb{R}^M$ is the spectral vector of the ith pixel. Suppose that the additive mixed noise is considered, the noise-perturbed degradation model [42] can be signified as $\mathbf{Y} = \mathbf{C} + \mathbf{S} + \mathbf{N}$, where $\mathbf{C} \in \mathbb{R}^{M\times L}$ is the clean image; $\mathbf{S} \in \mathbb{R}^{M\times L}$ denotes the sparse noise (i.e., salt and pepper noise and stripes noise); $\mathbf{N} \in \mathbb{R}^{M\times L}$ is the Gaussian noise or error residual. Since the pure hyperspectral data can be factorized into the product of endmember and abundance matrices using the linear mixed model (LMM), i.e., $\mathbf{C} = \mathbf{AX}$ [43], then the noise-perturbed degradation model is presented as

$$\mathbf{Y} = \mathbf{AX} + \mathbf{S} + \mathbf{N} \tag{1}$$

where $\mathbf{A} \in \mathbb{R}^{M\times N}$ represents the endmember matrix, containing N endmembers and M spectral bands; $\mathbf{X} \in \mathbb{R}^{N\times L}$ is the abundance matrix, each column of which represents the fractional proportions of N endmembers in each pixel. Following the minimization rule of error residual, Equation (1) can be reformulated as an unregularized optimization problem.

$$\begin{aligned} &\min_{\mathbf{A},\mathbf{X},\mathbf{S}} \ \frac{1}{2}\|\mathbf{Y} - \mathbf{AX} - \mathbf{S}\|_F^2 \\ &\text{s.t. } \mathbf{A} \succeq 0, \mathbf{X} \succeq 0 \end{aligned} \tag{2}$$

where two constraints require that each element in both endmember and abundance matrices is non-negative. However, it is an ill-posed inverse problem to reconstruct a clean image by the degradation data, which can be addressed by introducing prior information or regularization. Thus, this paper incorporates the piecewise weighted smoothing and sparse regularization to redefine the restoration model as

$$\begin{aligned} &\min_{\mathbf{A},\mathbf{X},\mathbf{S}} \ \frac{1}{2}\|\mathbf{Y} - \mathbf{AX} - \mathbf{S}\|_F^2 + \lambda_x\theta_x(\mathbf{X}) + \lambda_s\theta_s(\mathbf{S}) \\ &\text{s.t. } \mathbf{A} \succeq 0, \mathbf{X} \succeq 0 \end{aligned} \tag{3}$$

where $\theta_x(\mathbf{X})$ and $\theta_s(\mathbf{S})$ correspond to the regularization terms imposed on abundance matrix $\mathbf{X}$ and sparse noise $\mathbf{S}$, respectively; λ_x and λ_s are the weights.

B. SPARSE REGULARIZATION

According to sparse representation theory, the non-convex function l_0-norm represents the number of non-zero elements, but it is a NP-hard problem. As the surrogate of l_0-norm, l_1-norm and l_q-norm ($0 < q < 1$) are usually employed to promote sparsity. When l_q-norm is not less than $1/2$, the smaller the value of q is, the sparser the results are. On the contrary, it's not sensitive to the sparsity of the solutions when q lower than $1/2$. Therefore, $l_{1/2}$-norm is utilized as the sparse regularization in this article [44], defined as

$$\min_{\mathbf{X}} \ \lambda\|\mathbf{X}\|_{1/2} + \rho\|\mathbf{X} - \mathbf{B}\|_F^2 \tag{4}$$

Although problem (4) is non-convex, it can be solved by half thresholding operator to obtain the solution as follows.

$$\begin{aligned} \mathbf{X}^* &= \text{shrink}(\mathbf{B}, \lambda/\rho) \\ &= \begin{cases} \frac{2}{3}\mathbf{B}(1 + \cos(\frac{2\pi}{3} - \frac{2}{3}\phi_\lambda(\mathbf{B}))), & |\mathbf{B}| > \frac{\sqrt[3]{54}}{4}(\lambda/\rho)^{2/3} \\ 0, & \text{otherwise} \end{cases} \end{aligned} \tag{5}$$

where $\phi_\lambda(\mathbf{B}) = \arccos(\frac{\lambda}{8}(\frac{|\mathbf{B}|}{3})^{-3/2})$.

C. PIECEWISE WEIGHTED SMOOTHING REGULARIZATION ON ABUNDANCE MATRIX

Owing to local similarity, there exists a mass of redundant information scattered in the spatial subspace, which often results in the performance degradation of restoration image. However, it is relatively concentrated in transform domain, which can be easily handled to suppress the redundant information. Compared with traditional wavelet transform, tight framelet have higher redundancy, direction selectivity, shift invariance and robustness. Therefore, tight framelet transform is leveraged to handle the image restoration. More specifically, the analysis operator of discrete linear B-spline tight framelet transform for 1-D data can be defined as

$$\mathbf{W} = \begin{bmatrix} \mathbf{W}_1 \\ \mathbf{W}_2 \\ \mathbf{W}_3 \end{bmatrix} \tag{6}$$

where $\mathbf{W}_1$ represents the linear convolution operator of low-pass framelet filter $\mathbf{h}_1$ under Neumann boundary condition [45]; $\mathbf{W}_1$ and $\mathbf{W}_2$ denote linear convolution operator of band-pass filter $\mathbf{h}_2$, and high-pass filter $\mathbf{h}_3$, respectively. The framelet filters for 2-D data can be constructed via tensor product of 1-D framelet filters (i.e., $\mathbf{h}_{(1,1)} = \mathbf{h}_1 \otimes \mathbf{h}_1$). On this basis, a transform matrix $\mathbf{W}$ for 2-D image is denoted as $\mathbf{W} = [\mathbf{W}_{(1,1)}^T, \mathbf{W}_{(1,2)}^T, \ldots, \mathbf{W}_{(3,3)}^T]^T$, where $\mathbf{W}_{(p,q)}$ is the convolution operator of filter $\mathbf{h}_{(p,q)}$, and (p, q) denote the coordinates of different frequency components. Meanwhile, the synthesis transform of tight framelet is defined as the transpose of $\mathbf{W}$. A specific framelet domain based numerical example is shown below. For digital data $\mathbf{B} \in \mathbb{R}^N$, its corresponding framelet transform is $\mathbf{WB} \in \mathbb{R}^{9N}$, where $\mathbf{W} \in \mathbb{R}^{9N\times N}$. Furthermore, the most important property of tight framelet is $\mathbf{W}^T\mathbf{W} = \mathbf{I}$ [46].

After tight framelet transformation, the results of hyperspectral image in frequency domain are distributed in Fig. 1. We can observe that the principal components are mainly gathered in the low-frequency band, while the noise and details are presented in the high-frequency part. Furthermore, the higher frequency, the less detail there is in the figure. Meanwhile, in order to highlight the information in different frequency, the piecewise weighted coefficient is defined as

$$\lambda_{x_{(p,q)}} = \alpha e^{\text{dist}(p,q)} \tag{7}$$

where α is the baseline weight of low-frequency component; $\text{dist}(p, q) = \frac{1}{\sqrt{(p-1)^2+(q-1)^2}}$ denotes the Euclidean distance between two sub-blocks $\mathbf{W}_{(p,q)}$ and $\mathbf{W}_{(1,1)}$ in tight

framelet domain. In addition, the weights of the matrices on each subdiagonal are uniformly set to the Euclidean distance between the matrix on the edge of the subdiagonal and the low-frequency component. So the piecewise weighted smoothing regularization on abundance matrix can be defined as $\|\boldsymbol{\lambda}_x \odot \mathbf{WX}\|_{1/2}$, where $\boldsymbol{\lambda}_x = [\lambda_{x_{(1,1)}} \times \mathbf{1}_{W_{(1,1)}}, \lambda_{x_{(1,2)}} \times \mathbf{1}_{W_{(1,2)}}, \ldots, \lambda_{x_{(3,3)}} \times \mathbf{1}_{W_{(3,3)}}]^T$ denotes the corresponding weight matrix of the different frequency components in tight framelet, and $l_{1/2}$-norm is utilized to achieve piecewise smoothing in transform domain.

III. SOLVING ALGORITHM

The restoration model (2) is nonconvex for $(\mathbf{A}, \mathbf{X}, \mathbf{S})$, but it is a convex problem of single variable when the other two are fixed. Therefore, the model can be decoupled into three convex univariate subproblems using proximal alternating optimization (PAO), which are then updated iteratively until convergence.

$$\begin{aligned}\mathbf{X}^{k+1} \in \arg\min_{\mathbf{X}\geq 0} &\frac{1}{2}\|\mathbf{Y}-\mathbf{A}^k\mathbf{X}-\mathbf{S}^k\|_F^2 + \|\boldsymbol{\lambda}_x \odot \mathbf{WX}\|_{1/2} \\ &+\iota_+(\mathbf{X}) + \frac{\rho}{2}\left\|\mathbf{X}-\mathbf{X}_f\right\|_F^2 \qquad (8a)\\ \mathbf{A}^{k+1} \in \arg\min_{\mathbf{A}\geq 0} &\frac{1}{2}\left\|\mathbf{Y}-\mathbf{AX}^{k+1}-\mathbf{S}^k\right\|_F^2 + \iota_+(\mathbf{A}) \\ &+\frac{\rho}{2}\left\|\mathbf{A}-\mathbf{A}_f\right\|_F^2 \qquad (8b)\\ \mathbf{S}^{k+1} \in \arg\min_{\mathbf{S}} &\frac{1}{2}\left\|\mathbf{Y}-\mathbf{A}^{k+1}\mathbf{X}^{k+1}-\mathbf{S}\right\|_F^2 + \lambda_s\|\mathbf{S}\|_{1/2} \\ &+\frac{\rho}{2}\left\|\mathbf{S}-\mathbf{S}_f\right\|_F^2 \qquad (8c)\end{aligned}$$

where k represents the number of alternate iterations; $\mathbf{X}_f, \mathbf{A}_f$ and $\mathbf{S}_f$ indicate the values of $\mathbf{X}, \mathbf{A}$ and $\mathbf{S}$ in the previous iteration, respectively; $\iota_+(\mathbf{A})$ is an indicator function of non-negative variable, defined as

$$\iota_+(\mathbf{A}) = \begin{cases} 0, & \text{all } \mathbf{A}_{i_1,i_2} \geq 0 \\ +\infty, & \text{otherwise}. \end{cases} \qquad (9)$$

To sum up, the procedure of HSI restoration based on piecewise weighted smoothing in tight framelet domain is exhibited in Algorithm 1.

Algorithm 1 Piecewise Weighted Smoothing Regularization in Tight Framelet Domain

Input: $\mathbf{Y}, \lambda_x, \lambda_s, \rho, \beta$;
Initialize: $\mathbf{A}^0, \mathbf{X}^0, \mathbf{S}^0, k = 0$;
while the stopping criterion is not met **do**
  update $\mathbf{X}^{k+1}$ by (8a);
  update $\mathbf{A}^{k+1}$ by (8b);
  update $\mathbf{S}^{k+1}$ by (8c);
  $k = k + 1$;
end while
Output $\mathbf{C} = \mathbf{AX}$.

A. SOLUTION OF ABUNDANCE MATRIX

In the convex subproblem (8a) of abundance matrix, it contains piecewise weighted smoothing and non-negative regularization in tight framelet domain. Using ADMM, the equation constraints of $\mathbf{X}$ are set to conduct variable splitting. Thus, subproblem (8a) can be reformulated as

$$\begin{aligned}\min_{\mathbf{X},\mathbf{U},\boldsymbol{\eta}} &\frac{1}{2}\|\mathbf{Y}-\mathbf{AX}-\mathbf{S}\|_F^2 + \|\boldsymbol{\lambda}_\mathbf{x} \odot \mathbf{U}\|_{1/2} + \iota_+(\boldsymbol{\eta}) \\ &+\frac{\rho}{2}\left\|\mathbf{X}-\mathbf{X}_f\right\|_F^2 \qquad (10)\\ \text{s.t. } &\mathbf{U} = \mathbf{WX}, \boldsymbol{\eta} = \mathbf{X}\end{aligned}$$

The augmented Lagrangian function is given as

$$\begin{aligned}&L(\mathbf{X}, \mathbf{U}, \boldsymbol{\eta}, \mathbf{D}, \boldsymbol{\Lambda}) \\ &= \frac{1}{2}\|\mathbf{Y}-\mathbf{AX}-\mathbf{S}\|_F^2 + \|\boldsymbol{\lambda}_\boldsymbol{x} \odot \mathbf{U}\|_{1/2} + \iota_+(\boldsymbol{\eta}) \\ &\quad+\frac{\beta}{2}\left\|\mathbf{WX}-\mathbf{U}+\frac{\mathbf{D}}{\beta}\right\|_F^2 + \frac{\rho}{2}\left\|\mathbf{X}-\mathbf{X}_f\right\|_F^2 \\ &\quad+\frac{\beta}{2}\left\|\mathbf{X}-\boldsymbol{\eta}+\frac{\boldsymbol{\Lambda}}{\beta}\right\|_F^2 \qquad (11)\end{aligned}$$

where $\mathbf{D}, \boldsymbol{\Lambda}$ are dual variables, and β is the augmented Lagrangian coefficient. Via convex optimization tools, the closed-form solutions of all primal and dual variables can be obtained as

$$\begin{aligned}\mathbf{X}^{j+1} &= \left(\mathbf{A}^T\mathbf{A} + (\rho+2\beta)\mathbf{I}\right)^{-1}\left[\beta(\mathbf{W}^T\mathbf{U}^j + \boldsymbol{\eta}^j)\right. \\ &\quad\left.+\mathbf{A}^T(\mathbf{Y}-\mathbf{S}) + \rho\mathbf{X}_f - \mathbf{W}^T\mathbf{D}^j - \boldsymbol{\Lambda}^j\right] \qquad (12a)\\ \mathbf{U}^{j+1} &= \text{shrink}(\mathbf{WX}^{j+1} + \frac{\mathbf{D}^j}{\beta}, \frac{\boldsymbol{\lambda}_x}{\beta}) \qquad (12b)\\ \boldsymbol{\eta}^{j+1} &= \max(\mathbf{X}^{j+1} + \frac{\boldsymbol{\Lambda}^j}{\beta}, 0) \qquad (12c)\\ \mathbf{D}^{j+1} &= \mathbf{D}^j + \beta(\mathbf{WX}^{j+1} - \mathbf{U}^{j+1}) \qquad (12d)\\ \boldsymbol{\Lambda}^{j+1} &= \boldsymbol{\Lambda}^j + \beta(\mathbf{X}^{j+1} - \boldsymbol{\eta}^{j+1}) \qquad (12e)\end{aligned}$$

where j represents the iteration number (called inner loop).

B. SOLUTION OF ENDMEMBER MATRIX

Similar to abundance matrix, the equality constraint is used via ADMM to split the variable of endmember matrix. Thus, the subproblem (8b) of variable $\mathbf{A}$ is rewritten as

$$\begin{aligned}\min_{\mathbf{A},\mathbf{V}} &\frac{1}{2}\|\mathbf{Y}-\mathbf{AX}-\mathbf{S}\|_F^2 + \iota_+(\mathbf{V}) + \frac{\rho}{2}\left\|\mathbf{A}-\mathbf{A}_f\right\|_F^2 \\ \text{s.t. } &\mathbf{V} = \mathbf{A} \qquad (13)\end{aligned}$$

We can also obtain the closed-form solutions of primal and dual variables, which are presented as

$$\begin{aligned}\mathbf{A}^{j+1} &= \left[(\mathbf{Y}-\mathbf{S})\mathbf{X}^T + \rho\mathbf{A}_f + \beta\mathbf{V}^j - \mathbf{M}^j\right] \\ &\quad\left(\mathbf{XX}^T + (\rho+\beta)\mathbf{I}\right)^{-1} \qquad (14a)\end{aligned}$$

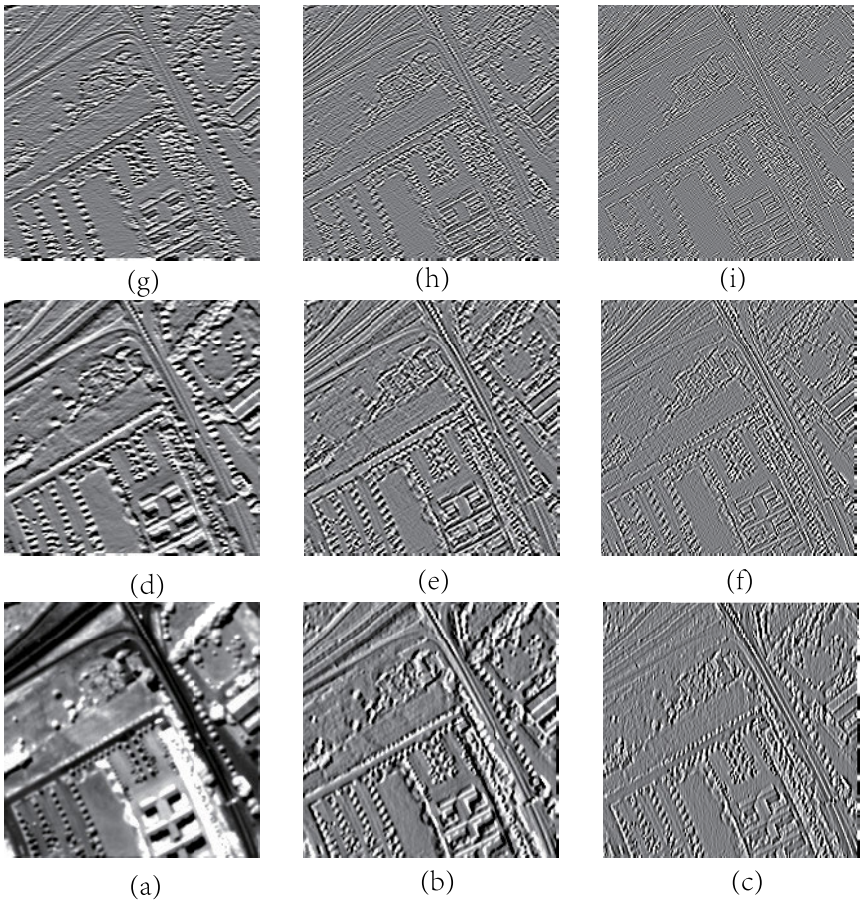

FIGURE 1. Tight framelet decomposition results at 100th band of Pavia University dataset: (a) Low frequency approximation in tight framelet domain, (b)-(i) High frequency in tight framelet domain.

$$\mathbf{V}^{j+1} = \max\left(\mathbf{A}^{j+1} + \frac{\mathbf{M}^j}{\beta}, 0\right) \tag{14b}$$

$$\mathbf{M}^{j+1} = \mathbf{M} + \beta\left(\mathbf{A}^{j+1} - \mathbf{V}^{j+1}\right) \tag{14c}$$

where $\mathbf{M}$ represents the dual variable.

C. SOLUTION OF SPARSE NOISE

For the convex subproblem of sparse noise $\mathbf{S}$, the corresponding closed-form solutions are expressed as

$$\mathbf{S}^{j+1} = \text{shrink}(\frac{\mathbf{Y} - \mathbf{AX} + \rho\mathbf{S}}{1+\rho}, \frac{\lambda_s}{1+\rho}) \tag{15}$$

D. STOPPING RULE

The stopping rule satisfies the relative difference value between the successive updates of the objective function $f(\mathbf{X}, \mathbf{A})$ is less than 0.01, that is,

$$f(\mathbf{X}, \mathbf{A}) = \frac{\|\mathbf{A}^{k+1}\mathbf{X}^{k+1} - \mathbf{A}^k\mathbf{X}^k\|_F}{\|\mathbf{A}^k\mathbf{X}^k\|_F} < 0.01 \tag{16}$$

The error setting for stopping the iteration is usually noise dependent, for example, 0.01 for a SNR of 20dB. Besides these, it is found that the inner loop iterations of $\mathbf{X}$, $\mathbf{A}$ and $\mathcal{S}$ does not need to run exhaustively for convergence, which has almost no impact on the overall performance. Therefore, the iterations of inner loops is set to within 5 times.

IV. EXPERIMENTAL SIMULATIONS AND PERFORMANCE ANALYSIS

To evaluate the performance of our algorithm for hyperspectral image restoration, several typical synthetic and real datasets are leveraged to perform the experimental simulations. Among them, synthetic datasets need to artificially add mixed noise, while real data has no extra noise. Furthermore, several performance metrics are adopted to estimate the quality, including PSNR (Peak signal to noise ratio) [47], SSIM (Structural similarity) [48], SAM (Spectral angle mapping) [49] and ERGAS (Relative dimensionless global error) [50]. In addition, the runtime (seconds) is also considered as the index to compute complexity. Especially, five state-of-the-art methods are employed as the baselines to conduct performance comparison, including deep-learning-based HySuDeep (Subspace representation and deep CNN Image prior) [15], tensor-decomposition-based LRTDGS (Weighted group sparsity-regularized low-rank tensor decomposition) [24], matrix-factorization-based E-3DTV (Enhanced 3-D total

variation) [36], SNLRSF (Subspace-based nonlocal low-Rank and sparse factorization method) [33] and F-LRNMF (Framelet-regularized low-rank nonnegative matrix factorization method) [34].

A. EXPERIMENTAL SIMULATIONS

1) SYNTHETIC DATASETS

There are two synthetic datasets with mixed noise in the experiments. To be specific, the first dataset is Washington DC Mall, acquired by hyperspectral digital image acquisition sensor. A sub-scene of size $191 \times 256 \times 256$ is selected as the region of interest (ROI) in this experiment. The second dataset was obtained at Pavia University, in northern Italy, in which a block of size $103 \times 200 \times 200$ was used in the experiment. Meanwhile, the values of parameter $\alpha, \lambda_S, \rho, \beta$ in the proposed algorithm are set to 10, 0.07, 0.1, and 10, respectively. The details are given in (IV-C).

2) NOISE SETTING

Generally, in the process of hyperspectral acquisition, it is inevitable to be polluted by a variety of noise, including Gaussian noise, sparse noise (i.e., salt and pepper noise, stripes noise), and others. To evaluate the restoration performance, four cases are set to simulate different noise environments by grouping sparse noise and Gaussian noise with different parameters (i.e., proportions or standard deviations). Then, in each case, two subcases are further designed to test the performance by fixing one kind of noise as follows.

Case I (Gaussian noise & different proportions of sparse noise): In two subcases, zero-mean Gaussian noise with standard deviation of 0.05 is added to all bands (i.e., $\sigma = 0.05$), while the proportions of salt and pepper noise are set to 0.2 and 0.3, separately (i.e., $\Psi = 0.2$).

Case II (Different standard deviations of Gaussian noise & sparse noise): The standard deviation of zero-mean Gaussian noise in two subcases are set to $\sigma = 0.05, 0.1$, separately. Meanwhile, the proportion of salt and pepper noise is fixed to $\Psi = 0.1$.

Case III (Random Gaussian noise & sparse noise): In one subcase, the standard deviation σ of zero-mean Gaussian noise is randomly generated from 0.05 to 0.1. Meanwhile, the proportion of salt and pepper noise is set to $\Psi = 0.1$; In the other one, the random standard deviation σ of Gaussian noise varies from 0.075 to 0.15 for all bands, while the proportion of salt and pepper noise is set to $\Psi = 0.1$.

Case IV (Gaussian noise & mixed sparse noise): In two subcases, the zero-mean Gaussian noise is fixed to $\sigma = 0.05$, and the proportion of salt and pepper noise is prescribed as $\Psi = 0.1$. Moreover, stripes noise is utilized to corrupt the randomly selected bands of synthetic dataset, where the distribution ratios of bands randomly polluted by 1 to 3 stripes noise are set to 0.1 and 0.5 separately (i.e., $\Omega = 0.1$ and $\Omega = 0.5$).

3) ANALYSIS OF RESTORATION IMAGES

The datasets of Washington DC Mall and Pavia University are utilized to test the visualization performance of the proposed PWSR-TF and the baselines, where the close-ups of restored images are shown in a red box. On the one hand, the reconstructed images of Washington DC Mall in Cases II and IV are shown in Figs. 2 and 3. One can obviously observe that the reconstructed image of proposed PWSR-TF retains more clear details than that of the baselines. On the other hand, Figs. 5 and 6 are the restored images of Pavia University in Case I and III. Distinctly, F-LRNMF and the proposed PWSR-TF have high similarity with the original image, which demonstrates the effectiveness of these methods in denoising. Besides restoration images, the further performance comparison between the reconstruction methods can also be illustrated in the following tables and curves. In a nutshell, the proposed PWSR-TF preserves more essential structures of clean hyperspectral image than the baselines.

4) ANALYSIS OF PERFORMANCE METRICS

The overall performances of two datasets under four noise conditions for all algorithms are shown in Tables 1, 2 and 3, 4. In addition, the item "Noisy" in tables denotes the performance of noise-corrupted image versus clean data without any processing. For the dataset of Washington DC Mall, the proposed PWSR-TF distinctly outperforms the benchmark algorithms. To be specific, compared with F-LRNMF, PSNR of our PWSR-TF is increased by more than 1dB, and ERGAS decreases approximately by 10%. In addition, other metrics can also be ameliorated outstandingly. Regarding to the Pavia University dataset, the proposed PWSR-TF provides higher-quality performance than the benchmark methods in all performance metrics, which verifies the validation of the proposed algorithm in this article.

5) ANALYSIS OF PERFORMANCE CURVES

The curves of PSNR and ERGAS with respect to spectral bands are drew in Figs. 4 and 7. It's obvious that the proposed PWSR-TF yields higher PSNR than the baseline methods in almost all bands. Meanwhile, one can see from Figs. 4 and 7 that the ERGAS of our PWSR-TF is more closed to 0 (ideal value) than that of the benchmarks for Washington DC Mall and Pavia University datasets. In conclusion, the proposed PWSR-TF makes significant improvements over the baseline algorithms in different bands for all cases.

B. REAL DATASETS

Two real datasets directly obtained in the practical application, are employed to verify the restoration performance of proposed PWSR-TF without artificially adding noise. One is the Urban dataset[1] acquired by the HYDICE (Hyperspectral Digital Imagery Collection Experiment) sensor, which has the size of $300 \times 300 \times 210$. The other is the Indian Pines

[1] http://www.tec.army.mil/hypercube

TABLE 1. Performance comparison of reconstructed images on Washington DC Wall (the best result highlighted in bold).

Case	Gaussian noise	Salt and pepper noise	Indicator	Noisy	HySuDeep	LRTDGS	E-3DTV	SNLRSF	F-LRNMF	Proposed
Case I	0.05	0.2	PSNR	11.37	29.41	34.24	33.26	34.84	37.82	**38.91**
			SSIM	0.129	0.899	0.938	0.935	0.956	0.976	**0.980**
			SAM	0.788	0.194	0.069	0.100	0.089	0.055	**0.049**
			ERGAS	1079.01	140.57	72.57	85.80	75.61	51.05	**43.89**
Case I	0.05	0.3	PSNR	9.66	28.11	33.88	35.13	29.53	36.43	**37.78**
			SSIM	0.080	0.856	0.934	0.924	0.843	0.971	**0.976**
			SAM	0.841	0.205	0.072	0.073	0.154	0.060	**0.054**
			ERGAS	1316.43	155.17	75.82	73.43	157.98	54.98	**49.67**
Case II	0.05	0.1	PSNR	14.25	29.91	34.46	34.62	37.66	38.61	**39.68**
			SSIM	0.248	0.911	0.941	0.948	0.972	0.980	**0.982**
			SAM	0.679	0.189	0.068	0.091	0.057	0.051	**0.045**
			ERGAS	775.97	136.38	70.97	62.58	49.78	47.21	**40.55**
Case II	0.1	0.1	PSNR	13.62	29.31	33.29	30.824	33.731	35.283	**36.352**
			SSIM	0.200	0.897	0.924	0.883	0.932	0.956	**0.964**
			SAM	0.707	0.191	0.078	0.122	0.087	0.072	**0.064**
			ERGAS	824.89	140.41	80.99	117.64	76.98	66.12	**57.73**

TABLE 2. Performance comparison of reconstructed images on Pavia University (the best result highlighted in bold).

Case	Gaussian noise	Salt and pepper noise	Indicator	Noisy	HySuDeep	LRTDGS	E-3DTV	SNLRSF	F-LRNMF	Proposed
Case I	0.05	0.2	PSNR	11.24	31.61	35.93	35.85	32.87	37.13	**38.17**
			SSIM	0.076	0.888	0.926	0.933	0.897	0.945	**0.956**
			SAM	0.833	0.107	0.068	0.069	0.111	0.071	**0.058**
			ERGAS	1116.27	113.76	65.42	68.01	112.76	60.53	**51.70**
Case I	0.05	0.3	PSNR	9.51	31.63	29.35	32.93	31.91	36.43	**37.54**
			SSIM	0.045	0.891	0.756	0.823	0.867	0.937	**0.952**
			SAM	0.877	0.103	0.164	0.079	0.172	0.073	**0.061**
			ERGAS	1363.71	120.41	134.68	244.96	149.43	64.38	**55.01**
Case II	0.05	0.1	PSNR	14.12	33.02	36.37	36.52	35.73	37.88	**39.07**
			SSIM	0.161	0.921	0.932	0.941	0.934	0.952	**0.961**
			SAM	0.727	0.100	0.065	0.066	0.071	0.071	**0.054**
			ERGAS	801.26	104.80	61.82	63.31	66.54	56.41	**47.17**
Case II	0.1	0.1	PSNR	13.53	31.84	33.99	33.94	33.93	34.64	**35.80**
			SSIM	0.124	0.894	0.892	0.899	0.851	0.911	**0.927**
			SAM	0.757	0.108	0.087	0.083	0.108	0.085	**0.072**
			ERGAS	853.45	111.95	80.76	83.33	103.81	76.72	**65.95**

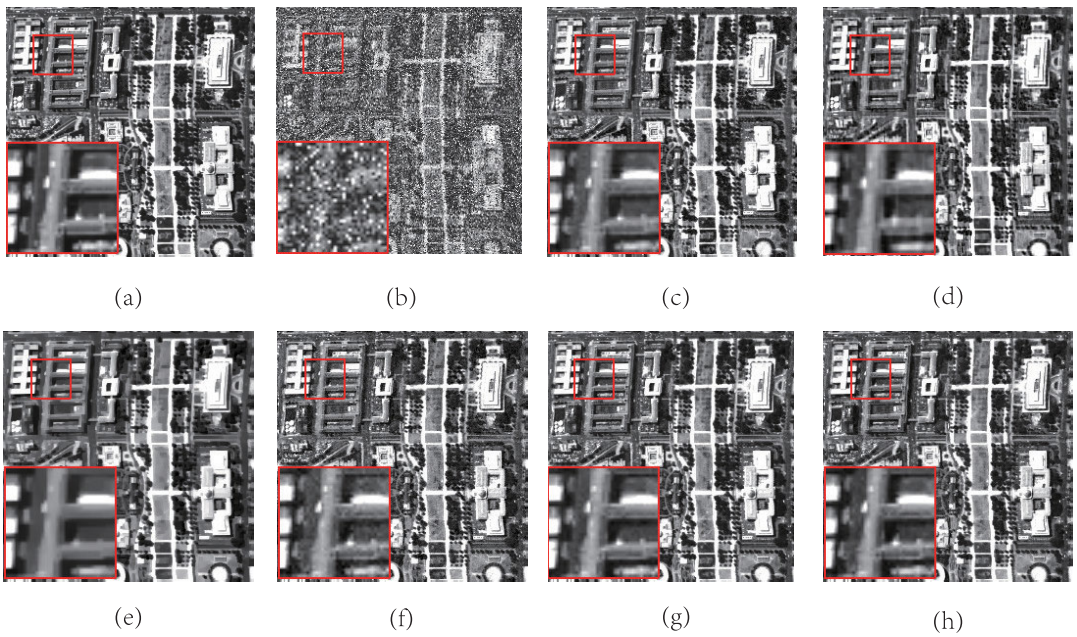

FIGURE 2. Restored images at the 50th band of Washington DC Mall in Case II ($\sigma = 0.1, \Psi = 0.1$), including: (a) Original image, (b) Noisy image, (c) HySuDeep, (d) LRTDGS, (e) E-3DTV, (f) SNLRSF, (g) F-LRNMF, (h) Proposed.

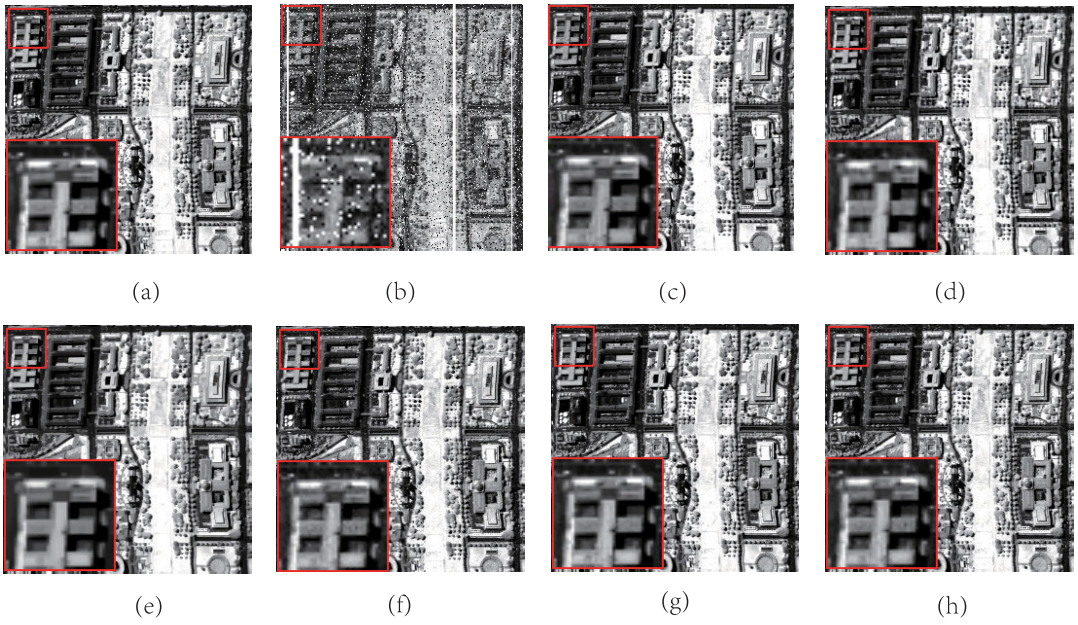

FIGURE 3. Restored images at the 70th band of Washington DC Mall in Case IV ($\sigma = 0.05, \Psi = 0.1, \omega = 0.5$), including: (a) Original image, (b) Noisy image, (c) HySuDeep, (d) LRTDGS, (e) E-3DTV, (f) SNLRSF, (g) F-LRNMF, (h) Proposed.

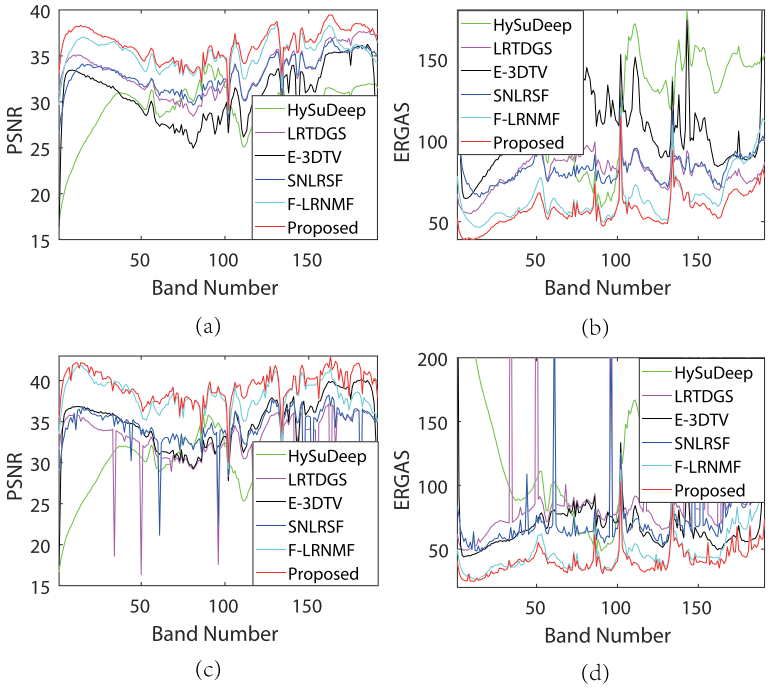

FIGURE 4. The PSNR and ERGAS curves with respect to spectral bands on Washington DC Mall under second subcase of different Case: (a)-(b) for Case II, (c)-(d) for Case IV.

dataset[2] obtained by the AVIRIS (Airborne Visible Infrared Imaging Spectrometer) sensor, containing 162 spectral bands and 145 × 145 pixels. Especially, both of datasets are liable to some noise during the course of image acquisition. The parameter settings in the real dataset experiment are identical to those in the synthetic dataset.

1) URBAN DATASET

The reconstructed images are shown in Fig. 8 by the proposed PWSR-TF and the benchmark algorithms. From the close-ups in red box of Fig. 8, we can observe that the benchmark

[2]https://engineering.purdue.edu/ biehl/MultiSpec/hyperspectral.html

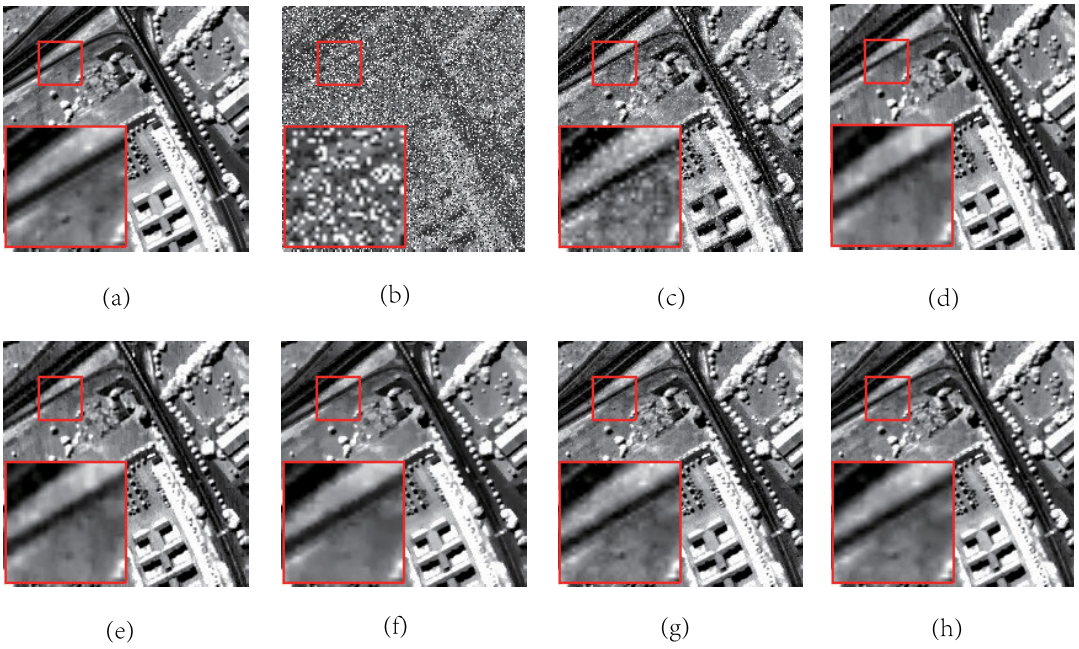

FIGURE 5. Restored images at the 100th band of Pavia University in Case I ($\sigma = 0.05$, $\Psi = 0.3$), including: (a) Original image, (b) Noisy image, (c) HySuDeep, (d) LRTDGS, (e) E-3DTV, (f) SNLRSF, (g) F-LRNMF, (h) Proposed.

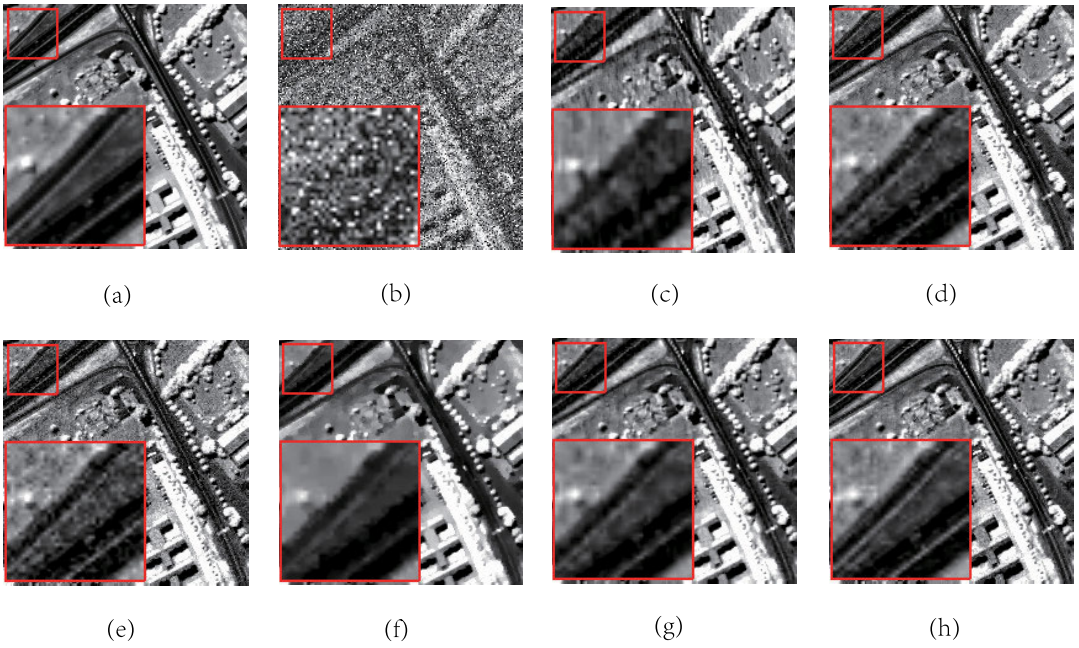

FIGURE 6. Restored images at the 100th band of Pavia University in Case III (σ is change from 0.075 to 0.15, $\Psi = 0.1$), including: (a) Original image, (b) Noisy image, (c) HySuDeep, (d) LRTDGS, (e) E-3DTV, (f) SNLRSF, (g) F-LRNMF, (h) Proposed.

algorithms of HySuDeep, SNLRSF and E-3DTV produce the low-quality performance in retaining local details. On the contrary, the proposed PWSR-TF, as well as LRTDGS and F-LRNMF, has high similarity in the aspect of clear reconstructed images, which indicates the three methods produce better restored results. The further comparison can employ the below performance metric.

Owing to lack ground-truth image as the reference image, this paper uses the horizontal mean profile as performance metric. Fig. 10 presents the horizontal mean profiles of the restored images for all algorithms, where the horizontal axis denotes the row number of Urban dataset in band of 210, and the vertical axis reflects the mean value of each row. In Fig. 10(a), it's pretty obvious that the original hyperspectral

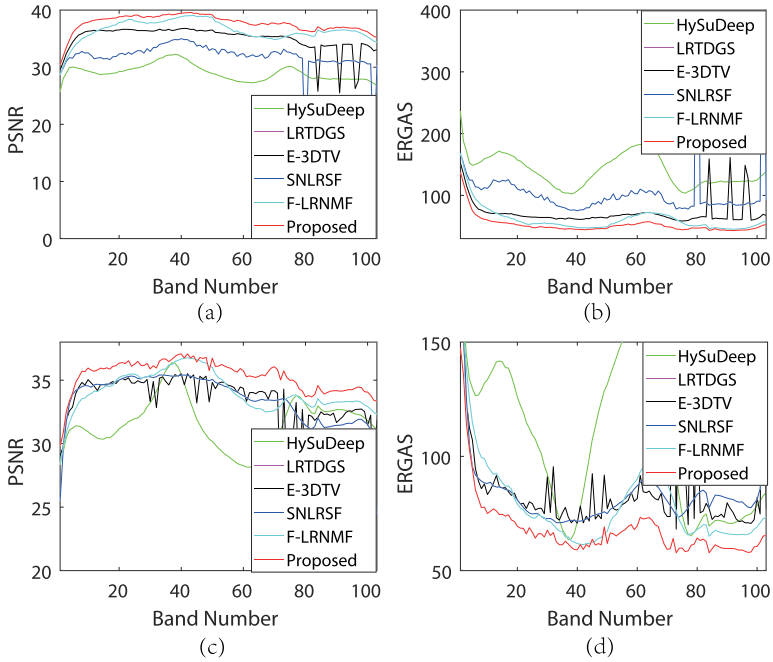

FIGURE 7. The PSNR and ERGAS curves with respect to spectral bands on Pavia University dataset under second subcase of different cases: (a)-(b) for Case I, (c)-(d) for Case III.

TABLE 3. Performance comparison of restoration methods on Washington DC dataset (the best result highlighted in bold).

Case	Gaussian noise	Salt and pepper noise	Stripes	Indicator	Noisy	HySuDeep	LRTDGS	E-3DTV	SNLRSF	F-LRNMF	Proposed
Case III	(0.05,0.1)	0.1	-	PSNR	13.97	29.63	33.91	33.31	35.59	36.87	**38.01**
				SSIM	0.225	0.905	0.933	0.933	0.955	0.970	**0.974**
				SAM	0.692	0.190	0.073	0.103	0.071	0.061	**0.055**
				ERGAS	797.02	137.99	75.51	62.75	56.27	**48.53**	55.22
Case III	(0.075,015)	0.1	-	PSNR	13.41	29.13	32.94	31.11	32.94	34.68	**35.70**
				SSIM	0.188	0.893	0.918	0.888	0.921	0.949	**0.958**
				SAM	0.717	0.192	0.083	0.123	0.094	0.076	**0.067**
				ERGAS	844.34	142.15	84.50	114.45	84.48	70.27	**61.94**
Case IV	0.05	0.1	0.1	PSNR	14.09	29.89	33.11	34.17	37.41	38.47	**39.64**
				SSIM	0.245	0.911	0.931	0.945	0.972	0.980	**0.982**
				SAM	0.684	0.189	0.109	0.092	0.058	0.051	**0.046**
				ERGAS	789.78	136.47	124.27	82.57	51.19	48.01	**40.53**
Case IV	0.05	0.1	0.5	PSNR	13.54	29.82	32.71	34.9	35.64	38.24	**39.32**
				SSIM	0.237	0.909	0.927	0.953	0.965	0.979	**0.982**
				SAM	0.704	0.188	0.117	0.097	0.073	0.053	**0.049**
				ERGAS	851.18	135.75	140.75	76.85	87.84	49.53	**43.26**

TABLE 4. Performance comparison of restoration methods on Pavia University (the best result highlighted in bold).

Case	Gaussian noise	Salt and pepper noise	Stripes	Indicator	Noisy	HySuDeep	LRTDGS	E-3DTV	SNLRSF	F-LRNMF	Proposed
Case III	(0.05,0.1)	0.1	-	PSNR	13.84	32.49	35.11	35.27	33.61	36.29	**37.50**
				SSIM	0.143	0.909	0.912	0.922	0.899	0.90	**0.948**
				SAM	0.743	0.104	0.077	0.074	0.111	0.075	**0.062**
				ERGAS	827.87	108.20	71.65	72.28	93.62	65.45	**55.22**
Case III	(0.75,0.15)	0.1	-	PSNR	13.34	31.59	33.39	33.50	31.38	34.08	**35.32**
				SSIM	0.116	0.889	0.876	0.891	0.849	0.901	**0.923**
				SAM	0.765	0.113	0.104	0.085	0.135	0.088	**0.074**
				ERGAS	870.75	113.58	88.84	87.16	119.11	81.385	**69.23**
Case IV	0.05	0.1	0.1	PSNR	13.93	33.01	34.81	36.42	35.05	37.85	**39.07**
				SSIM	0.159	0.921	0.915	0.939	0.924	0.972	**0.961**
				SAM	0.736	0.100	0.141	0.067	0.106	0.067	**0.054**
				ERGAS	824.59	104.91	176.01	64.15	109.51	56.51	**47.12**
Case IV	0.05	0.1	0.5	PSNR	13.18	32.90	34.11	36.62	33.28	37.48	**38.95**
				SSIM	0.152	0.919	0.898	0.941	0.908	0.951	**0.960**
				FSIM	0.766	0.101	0.229	0.066	0.112	0.070	**0.056**
				ERGAS	919.44	105.14	268.19	63.45	137.09	58.39	**47.77**

image has a rapid fluctuation, which indicates it is seriously interrupted by noise. While, the curve of proposed PWSR-TF is smoother than that of the benchmarks, which verifies it has better reconstructed performance.

2) INDIAN PINE DATASET

Fig. 9 showcases the restoration results of Indian Pine dataset yielded by all methods. One can distinctly observe that all of methods can remove mixed noise to various degrees. Further comparison of the details from restoration images, one can easily obtain the conclusion that the proposed PWSR-TF can preserve more details and image signatures. That is, it also verifies that piecewise weighted smoothing regularization in tight framelet domain has a certain advantage in retaining the local details.

To evaluate the restoration performance intuitively, we also draw the horizontal mean profiles of Indian Pine dataset. As shown in Fig. 11, the proposed PWSR-TF performs a smoother curve in the horizontal direction than the benchmark algorithms, which demonstrates our algorithm can effectively suppress mixed noise and yield high-fidelity restoration performance.

C. PARAMETER DISCUSSION

In this part, the parameter setting of the proposed PWSR-TF will be discussed, including the baseline weight of low-frequency component α, regularization parameter λ_S, proximal coefficient ρ, the estimated rank N, the augmented Lagrangian coefficient β and iteration number. In general, the weight is related to the noise level, for example, the weight is fixed to 0.01 when the whole SNR is 20 dB. For convenience, we take the second datasets in Case I as an example to conduct the experimental test and analysis.

1) PARAMETER α

In Equation (7), α denotes the baseline weight of low-frequency component, which has a significant effect on the weight of different frequency bands. Fig. 12(a) shows the performance of PSNR versus α, in which the proposed PWSR-TF increases rapidly when α changes from 1 to 10. With the increasing continuously of α, PSNR reduces slightly. To sum up, the baseline weight of low-frequency component α is set to 10.

2) PARAMETER λ_S

It's no doubt that λ_S can be available for promoting the sparsity of sparse noise. From Fig. 12(b), one can obtain the conclusion that the PSNR is improved significantly when λ_S varies from 0.01 to 0.07. As λ_S continues to increase, the variation of PSNR trends to be stable. Therefore, the value of λ_S in all experiments conducted by the proposed algorithm is fixed to 0.07.

3) PARAMETER ρ

Our PWSR-TF adopts the proximal term to enhance the convergence. Fig. 12(c) displays the performance curve of PSNR with respect to proximal parameter $\lg(\rho)$, which presents an obvious decrease since the value of ρ is 0.1. In consequence, we choose 0.1 as the proximal term parameter value.

4) PARAMETER N

The parameter N denotes the rank of endmember matrix, i.e., the number of substances underlying in the target image. The performance curve of PSNR with respect to N is depicted in Fig. 12(d). It can be easily observed that PSNR is not sensitive to N when the value of rank is not less than 10. According to the above analysis, the value of estimated rank N is set to 10.

5) PARAMETER β

Fig. 12(e) exhibits PSNR value sensitivity analysis of the augmented Lagrangian coefficient β. From the result, it can be easily observed that the value of PSNR approximates ideal result when the value of β equals to 10. Therefore, 10 is selected for β during whole experiment.

6) ITERATION NUMBER

The experiment is conducted to test the convergence of the proposed PWSR-TF. Fig. 13 displays the change curves of PSNR with respect to the iteration number in Washington DC Wall and Pavia University datasets under second subcases of Case II and Case IV, respectively. One can obviously see that, the value of PSNR acquires the approximation of steady result when the iterations reaches 40, which demonstrates the proposed algorithm has ideal convergence.

D. ABLATION STUDY

In this subsection, two ablation experiments are carefully designed to testify the validation of transform and weighting employed in our paper.

1) TRANSFORM DOMAIN

To objectively demonstrate the effectiveness of different transforms, we perform an ablation experiment by employing wavelet transform and cubic B-spline framelet transform(denoted as C-framelet) to replace linear B-spline framelet transform separately. Table 5 presents the restoration performances of ablation study on Washington DC Mall and Pavia University datasets. It can be observed that the restored results of proposed PWSR-TF is significantly better than that of the other two under various noise environments, which demonstrates the effectiveness of tight framelet in this paper.

2) WEIGHTING SCHEME

To verify the rationality of weighting schemes, a comparison experiment of constant weighting (C-W), high-low frequency weighting (H-L) and proposed piecewise weighting (PWSR-TF) is elaborately designed. Specifically, the definition of C-W is written as $\boldsymbol{\lambda_x} = [\lambda_{c-w} \times \mathbf{1}_{W_{(1,1)}}, \lambda_{c-w} \times \mathbf{1}_{W_{(1,2)}}, \ldots, \lambda_{c-w} \times \mathbf{1}_{W_{(3,3)}}]^T$. H-L applies different weights (i.e., λ_l and λ_h) to low frequency and high frequency

FIGURE 8. Restored results at 210th of Urban dataset, including: (a) Original image, (b) HySuDeep, (c) LRTDGS, (d) E-3DTV, (e) SNLRSF, (f) F-LRNMF, (g) Proposed.

FIGURE 9. Restored results at 1st of Indian Pine dataset, including: (a) Original image, (b) HySuDeep, (c) LRTDGS, (d) E-3DTV, (e) SNLRSF, (f) F-LRNMF, (g) Proposed.

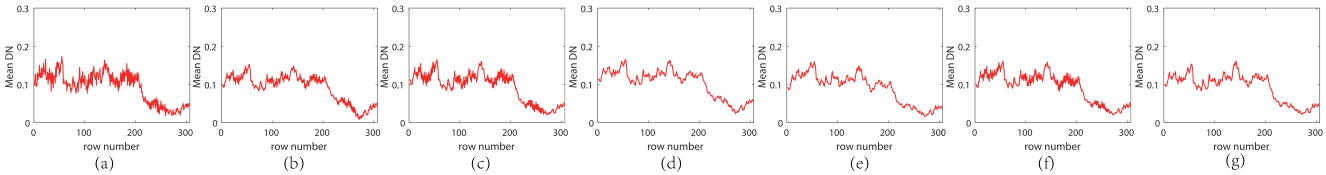

FIGURE 10. Horizontal profile at 200th of Urban dataset, including: (a) Original image, (b) HySuDeep, (c) LRTDGS, (d) E-3DTV, (e) SNLRSF, (f) F-LRNMF, (g) Proposed.

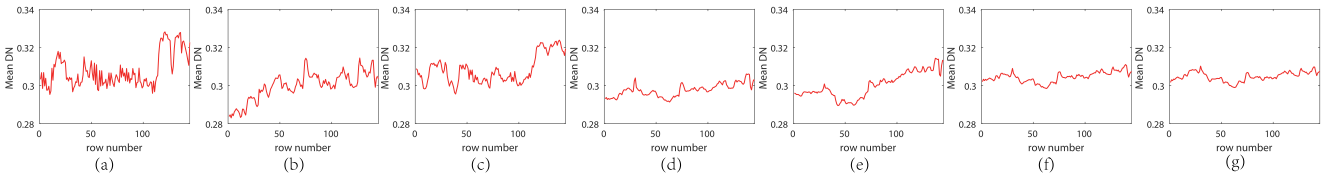

FIGURE 11. Horizontal profile at 1st of Indian Pine dataset, including: (a) Original image, (b) HySuDeep, (c) LRTDGS, (d) E-3DTV, (e) SNLRSF, (f) F-LRNMF, (g) Proposed.

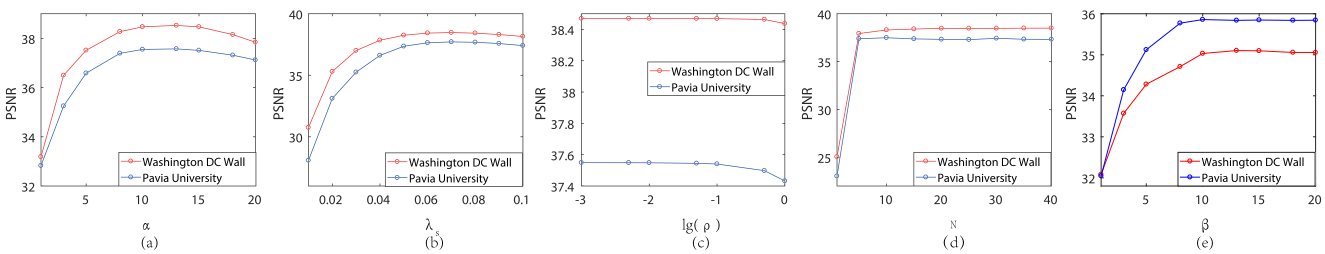

FIGURE 12. The performance PSNR with respect to the parameters separately, including: (a) α, (b) λ_s, (c) ρ, (d) N, (e) β.

separately, defined as $\boldsymbol{\lambda_x} = [\lambda_l \times \mathbf{1}_{W_{(1,1)}}, \lambda_h \times \mathbf{1}_{W_{(1,2)}}, \ldots, \lambda_h \times \mathbf{1}_{W_{(3,3)}}]^T$. Table 6 presents the optimal quantitative evaluation values of three weighting schemes on Washington DC Mall and Pavia University datasets under different noise settings. Compared with the other two weighting schemes, the proposed PWSR-TF achieves a more satisfactory restoration

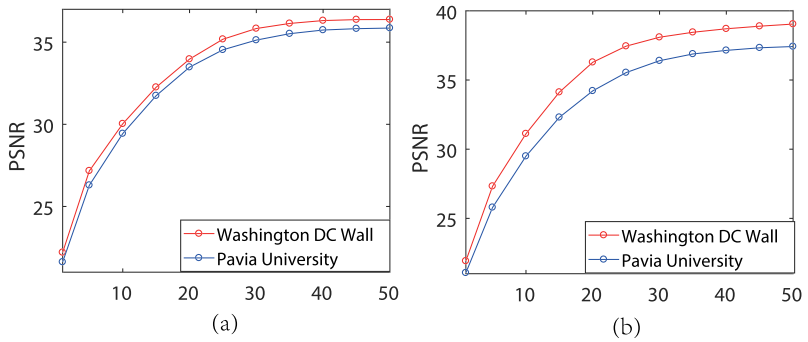

FIGURE 13. Relationship between iteration number and PSNR in different Case: (a) Case II, (b) Case V.

TABLE 5. Performance comparison of different transform domain.

Transform	*Dataset*	*Case*	Gaussian noise	Salt and pepper noise	Stripes	PSNR	SSIM	SAM	ERGAS
Wavelet	Washington DC	II	0.1	0.1	-	33.09	0.924	0.099	83.50
	Pavia University	II	0.1	0.1	-	32.26	**0.931**	0.095	80.05
	Washington DC	IV	0.05	0.1	0.5	35.80	0.961	0.071	63.40
	Pavia University	IV	0.05	0.1	0.5	34.41	0.906	0.103	90.41
C-framelet	Washington DC	II	0.1	0.1	-	33.28	0.916	0.102	81.75
	Pavia University	II	0.1	0.1	-	32.54	0.852	0.097	94.47
	Washington DC	IV	0.05	0.1	0.5	38.19	0.974	0.061	51.64
	Pavia University	IV	0.05	0.1	0.5	36.29	0.923	0.124	130.09
PWSR-TF	Washington DC	II	0.1	0.1	-	**36.35**	**0.964**	**0.064**	**57.73**
	Pavia University	II	0.1	0.1	-	**35.80**	0.927	**0.072**	**65.95**
	Washington DC	IV	0.05	0.1	0.5	**39.32**	**0.982**	**0.049**	**43.25**
	Pavia University	IV	0.05	0.1	0.5	**38.95**	**0.960**	**0.056**	**47.77**

TABLE 6. Performance comparison of different weighted method.

method	*Dataset*	*Case*	Gaussian noise	Salt and pepper noise	Stripes	PSNR	SSIM	SAM	ERGAS
C-W	Washington DC	II	0.1	0.1	-	35.39	0.953	0.076	64.93
	Pavia University	II	0.1	0.1	-	34.91	0.911	0.084	73.64
	Washington DC	IV	0.05	0.1	0.5	38.08	0.978	0.057	53.91
	Pavia University	IV	0.05	0.1	0.5	36.30	0.938	0.125	140.21
H-L	Washington DC	II	0.1	0.1	-	35.96	0.961	0.068	60.88
	Pavia University	II	0.1	0.1	-	35.49	0.925	0.075	68.21
	Washington DC	IV	0.05	0.1	0.5	38.86	0.980	0.051	44.27
	Pavia University	IV	0.05	0.1	0.5	37.17	0.948	0.086	83.58
PWSR-TF	Washington DC	II	0.1	0.1	-	**36.35**	**0.964**	**0.064**	**57.73**
	Pavia University	II	0.1	0.1	-	**35.80**	**0.927**	**0.072**	**65.95**
	Washington DC	IV	0.05	0.1	0.5	**39.32**	**0.982**	**0.049**	**43.25**
	Pavia University	IV	0.05	0.1	0.5	**38.95**	**0.960**	**0.056**	**47.77**

TABLE 7. Runtime comparison of restored algorithms.

datasets	runtime(s)					
	HySuDeep	LRTDGS	E-3DTV	SNLRSF	F-LRNMF	Proposed
Washington DC Mall	216.18	**110.63**	274.01	643.41	130.62	198.23
Pavia University	102.84	**35.94**	58.64	363.73	62.51	97.55
Urban	427.58	**108.91**	1694.60	998.42	188.54	287.45
Indian Pines	69.31	44.79	57.61	217.09	**42.05**	62.97

performance in most cases, which also certifies the rationality of piecewise weighting.

E. COMPUTATIONAL COMPLEXITY ANALYSIS

The main calculations of the proposed PWSR-TF are divided into $\mathbf{X}$, $\mathbf{A}$, and $\mathcal{S}$. Then the complexities of both equations (12a) and (14a) are equal to $\mathcal{O}(MNL)$, and the computation of (15) takes up to $\mathcal{O}(ML)$. Considering aforementioned equations together, the overall computational complexity of proposed PWSR-TF algorithm is $\mathcal{O}((2N+1)ML)$. Furthermore, the complexity of algorithm can also be effectively reflected by runtime. Specifically, the runtime of the proposed PWSR-TF and the baselines are shown in Table 7. We can observe that except LRTDGS and

F-LRNMF, the proposed PWSR-TF runs faster than the other three benchmark methods in almost all of the datasets, which demonstrates the proposed PWSR-TF needs to be further optimized in the future.

V. CONCLUSION

In this paper, a hyperspectral image restoration algorithm based on piecewise weighted smoothing regularization in tight framelet domain is proposed to remove mixed noise. On the basis of non-negative matrix decomposition, the abundance matrix in different frequency of tight framelet domain is imposed by corresponding weight, and l_q norm is employed as the sparsity regularization. Moreover, to construct the restoration model, we combine the tight framelet transformation algorithm with the alternating direction multiplier method to derive the closed form solutions. Using the synthetic and real datasets in the experiments, the test results illustrate that the proposed algorithm generates better performance in image restoration than the state-of-the-art baseline methods. In future plans, we will explore the influence of other multi-scale geometric methods on the piecewise smoothing regularization, and develop other effective solving algorithm to reduce the runtime.

REFERENCES

[1] C. Yu, J. Huang, M. Song, Y. Wang, and C.-I. Chang, "Edge-inferring graph neural network with dynamic task-guided self-diagnosis for few-shot hyperspectral image classification," *IEEE Trans. Geosci. Remote Sens.*, vol. 60, 2022, Art. no. 5535613.

[2] Z. Wu, H. Su, X. Tao, L. Han, M. E. Paoletti, J. M. Haut, J. Plaza, and A. Plaza, "Hyperspectral anomaly detection with relaxed collaborative representation," *IEEE Trans. Geosci. Remote Sens.*, vol. 60, 2022, Art. no. 5533417.

[3] Z. Wu, J. Sun, Y. Zhang, Z. Wei, and J. Chanussot, "Recent developments in parallel and distributed computing for remotely sensed big data processing," *Proc. IEEE*, vol. 109, no. 8, pp. 1282–1305, Aug. 2021.

[4] Z. Zeng, T.-Z. Huang, Y. Chen, and X.-L. Zhao, "Nonlocal block-term decomposition for hyperspectral image mixed noise removal," *IEEE J. Sel. Topics Appl. Earth Observ. Remote Sens.*, vol. 14, pp. 5406–5420, 2021.

[5] H. Sun, X. Zheng, and X. Lu, "A supervised segmentation network for hyperspectral image classification," *IEEE Trans. Image Process.*, vol. 30, pp. 2810–2825, 2021.

[6] P. D. Dao, K. Mantripragada, Y. He, and F. Z. Qureshi, "Improving hyperspectral image segmentation by applying inverse noise weighting and outlier removal for optimal scale selection," *ISPRS J. Photogramm. Remote Sens.*, vol. 171, pp. 348–366, Jan. 2021.

[7] F. Vincent and O. Besson, "Robust adaptive target detection in hyperspectral imaging," *Signal Process.*, vol. 181, Apr. 2021, Art. no. 107905.

[8] F. Xiong, J. Zhou, S. Tao, J. Lu, J. Zhou, and Y. Qian, "SMDS-Net: Model guided spectral-spatial network for hyperspectral image denoising," *IEEE Trans. Image Process.*, vol. 31, pp. 5469–5483, 2022.

[9] X. Kong, Y. Zhao, J. C.-W. Chan, and J. Xue, "Hyperspectral image restoration via spatial–spectral residual total variation regularized low-rank tensor decomposition," *Remote Sens.*, vol. 14, no. 3, p. 511, Jan. 2022.

[10] H. V. Nguyen, M. O. Ulfarsson, J. Sigurdsson, and J. R. Sveinsson, "Deep sparse and low-rank prior for hyperspectral image denoising," in *Proc. IEEE Int. Geosci. Remote Sens. Symp.*, Jul. 2022, pp. 1217–1220.

[11] Y.-C. Miao, X.-L. Zhao, X. Fu, J.-L. Wang, and Y.-B. Zheng, "Hyperspectral denoising using unsupervised disentangled spatiospectral deep priors," *IEEE Trans. Geosci. Remote Sens.*, vol. 60, 2022, Art. no. 5513916.

[12] H. Chen, G. Yang, and H. Zhang, "Hider: A hyperspectral image denoising transformer with spatial–spectral constraints for hybrid noise removal," *IEEE Trans. Neural Netw. Learn. Syst.*, early access, Oct. 31, 2022, doi: 10.1109/TNNLS.2022.3215751.

[13] O. Sidorov and J. Y. Hardeberg, "Deep hyperspectral prior: Single-image denoising, inpainting, super-resolution," in *Proc. IEEE/CVF Int. Conf. Comput. Vis. Workshop (ICCVW)*, Oct. 2019, pp. 1–15.

[14] W. Xie and Y. Li, "Hyperspectral imagery denoising by deep learning with trainable nonlinearity function," *IEEE Geosci. Remote Sens. Lett.*, vol. 14, no. 11, pp. 1963–1967, Nov. 2017.

[15] L. Zhuang, M. K. Ng, and X. Fu, "Hyperspectral image mixed noise removal using subspace representation and deep CNN image prior," *Remote Sens.*, vol. 13, no. 20, p. 4098, Oct. 2021.

[16] Y.-S. Luo, X.-L. Zhao, T.-X. Jiang, Y.-B. Zheng, and Y. Chang, "Hyperspectral mixed noise removal via spatial–spectral constrained unsupervised deep image prior," *IEEE J. Sel. Topics Appl. Earth Observ. Remote Sens.*, vol. 14, pp. 9435–9449, 2021.

[17] F. Xiong, J. Zhou, Q. Zhao, J. Lu, and Y. Qian, "MAC-Net: Model-aided nonlocal neural network for hyperspectral image denoising," *IEEE Trans. Geosci. Remote Sens.*, vol. 60, 2022, Art. no. 5519414.

[18] X. Bai, F. Xu, L. Zhou, Y. Xing, L. Bai, and J. Zhou, "Nonlocal similarity based nonnegative tucker decomposition for hyperspectral image denoising," *IEEE J. Sel. Topics Appl. Earth Observ. Remote Sens.*, vol. 11, no. 3, pp. 701–712, Mar. 2018.

[19] G. Fu, F. Xiong, J. Lu, J. Zhou, and Y. Qian, "Nonlocal spatial–spectral neural network for hyperspectral image denoising," *IEEE Trans. Geosci. Remote Sens.*, vol. 60, 2022, Art. no. 5541916.

[20] Y. Chen, W. He, N. Yokoya, T.-Z. Huang, and X.-L. Zhao, "Nonlocal tensor-ring decomposition for hyperspectral image denoising," *IEEE Trans. Geosci. Remote Sens.*, vol. 58, no. 2, pp. 1348–1362, 2020.

[21] F. Xiong, J. Zhou, and Y. Qian, "Hyperspectral restoration via ℓ_0 gradient regularized low-rank tensor factorization," *IEEE Trans. Geosci. Remote Sens.*, vol. 57, no. 12, pp. 10410–10425, 2019.

[22] Y. Chen, W. He, X.-L. Zhao, T.-Z. Huang, J. Zeng, and H. Lin, "Exploring nonlocal group sparsity under transform learning for hyperspectral image denoising," *IEEE Trans. Geosci. Remote Sens.*, vol. 60, 2022, Art. no. 5537518.

[23] F. Ma, S. Huo, and F. Yang, "Graph-based logarithmic low-rank tensor decomposition for the fusion of remotely sensed images," *IEEE J. Sel. Topics Appl. Earth Observ. Remote Sens.*, vol. 14, pp. 11271–11286, 2021.

[24] Y. Chen, W. He, N. Yokoya, and T.-Z. Huang, "Hyperspectral image restoration using weighted group sparsity-regularized low-rank tensor decomposition," *IEEE Trans. Cybern.*, vol. 50, no. 8, pp. 3556–3570, Aug. 2020.

[25] Y.-B. Zheng, T.-Z. Huang, X.-L. Zhao, Y. Chen, and W. He, "Double-factor-regularized low-rank tensor factorization for mixed noise removal in hyperspectral image," *IEEE Trans. Geosci. Remote Sens.*, vol. 58, no. 12, pp. 8450–8464, 2020.

[26] Y. Chen, Y. Guo, Y. Wang, D. Wang, C. Peng, and G. He, "Denoising of hyperspectral images using nonconvex low rank matrix approximation," *IEEE Trans. Geosci. Remote Sens.*, vol. 55, no. 9, pp. 5366–5380, 2017.

[27] Y. Xie, Y. Qu, D. Tao, W. Wu, Q. Yuan, and W. Zhang, "Hyperspectral image restoration via iteratively regularized weighted Schatten p-norm minimization," *IEEE Trans. Geosci. Remote Sens.*, vol. 54, no. 8, pp. 4642–4659, 2016.

[28] Y. Xie, S. Gu, Y. Liu, W. Zuo, W. Zhang, and L. Zhang, "Weighted Schatten p-norm minimization for image denoising and background subtraction," *IEEE Trans. Image Process.*, vol. 25, no. 10, pp. 4842–4857, Oct. 2016.

[29] Y.-B. Zheng, T.-Z. Huang, X.-L. Zhao, T.-X. Jiang, T.-H. Ma, and T.-Y. Ji, "Mixed noise removal in hyperspectral image via low-fibered-rank regularization," *IEEE Trans. Geosci. Remote Sens.*, vol. 58, no. 1, pp. 734–749, 2020.

[30] H. Fan, Y. Chen, Y. Guo, H. Zhang, and G. Kuang, "Hyperspectral image restoration using low-rank tensor recovery," *IEEE J. Sel. Topics Appl. Earth Observ. Remote Sens.*, vol. 10, no. 10, pp. 4589–4604, Oct. 2017.

[31] Y. Chen, T.-Z. Huang, W. He, X.-L. Zhao, H. Zhang, and J. Zeng, "Hyperspectral image denoising using factor group sparsity-regularized nonconvex low-rank approximation," *IEEE Trans. Geosci. Remote Sens.*, vol. 60, 2022, Art. no. 5515916.

[32] H. Zhang, W. He, L. Zhang, H. Shen, and Q. Yuan, "Hyperspectral image restoration using low-rank matrix recovery," *IEEE Trans. Geosci. Remote Sens.*, vol. 52, no. 8, pp. 4729–4743, 2013.

[33] C. Cao, J. Yu, C. Zhou, K. Hu, F. Xiao, and X. Gao, "Hyperspectral image denoising via subspace-based nonlocal low-rank and sparse factorization," *IEEE J. Sel. Topics Appl. Earth Observ. Remote Sens.*, vol. 12, no. 3, pp. 973–988, Mar. 2019.

[34] Y. Chen, T.-Z. Huang, X.-L. Zhao, and L.-J. Deng, "Hyperspectral image restoration using framelet-regularized low-rank nonnegative matrix factorization," *Appl. Math. Model.*, vol. 63, pp. 128–147, Nov. 2018.
[35] W. He, H. Zhang, L. Zhang, and H. Shen, "Total-variation-regularized low-rank matrix factorization for hyperspectral image restoration," *IEEE Trans. Geosci. Remote Sens.*, vol. 54, no. 1, pp. 178–188, 2016.
[36] J. Peng, Q. Xie, Q. Zhao, Y. Wang, D. Meng, and Y. Leung, "Enhanced 3DTV regularization and its applications on hyper-spectral image denoising and compressed sensing," 2018, *arXiv:1809.06591*.
[37] H. Zeng, X. Xie, and J. Ning, "Hyperspectral image denoising via global spatial–spectral total variation regularized nonconvex local low-rank tensor approximation," *Signal Process.*, vol. 178, Jan. 2021, Art. no. 107805.
[38] A. Paul, A. Kundu, N. Chaki, D. Dutta, and C. S. Jha, "Wavelet enabled convolutional autoencoder based deep neural network for hyperspectral image denoising," *Multimedia Tools Appl.*, vol. 81, no. 2, pp. 2529–2555, Jan. 2022.
[39] G. Zhang, Y. Xu, and F. Fang, "Framelet-based sparse unmixing of hyperspectral images," *IEEE Trans. Image Process.*, vol. 25, no. 4, pp. 1516–1529, Apr. 2016.
[40] Y.-B. Zheng, T.-Z. Huang, T.-Y. Ji, X.-L. Zhao, T.-X. Jiang, and T.-H. Ma, "Low-rank tensor completion via smooth matrix factorization," *Appl. Math. Model.*, vol. 70, pp. 677–695, Jun. 2019.
[41] C. Xu, Z. Wu, F. Li, S. Zhang, C. Deng, and Y. Wang, "Spectral–spatial joint sparsity unmixing of hyperspectral images based on framelet transform," *Infr. Phys. Technol.*, vol. 112, Jan. 2021, Art. no. 103564.
[42] Y. Hu and X. Li, "Hyperspectral image restoration using nonconvex hybrid regularization," in *Proc. IEEE Int. Geosci. Remote Sens. Symp.*, Jul. 2019, pp. 393–396.
[43] L. Miao and H. Qi, "Endmember extraction from highly mixed data using minimum volume constrained nonnegative matrix factorization," *IEEE Trans. Geosci. Remote Sens.*, vol. 45, no. 3, pp. 765–777, 2007.
[44] W. Cao, J. Sun, and Z. Xu, "Fast image deconvolution using closed-form thresholding formulas of $L_q(q = 1/2,2/3)$ regularization," *J. Vis. Commun. Image Represent.*, vol. 24, no. 1, pp. 31–41, Jan. 2013.
[45] J. F. Cai, S. Huang, H. Ji, Z. Shen, and G. Ye, "Data-driven tight frame construction and image denoising," *Appl. Comput. Harmon. Anal.*, vol. 37, no. 1, pp. 89–105, Jul. 2014.
[46] Y. Liu, Z. Zhan, J.-F. Cai, D. Guo, Z. Chen, and X. Qu, "Projected iterative soft-thresholding algorithm for tight frames in compressed sensing magnetic resonance imaging," *IEEE Trans. Med. Imag.*, vol. 35, no. 9, pp. 2130–2140, Sep. 2016.
[47] L. Pang, W. Gu, and X. Cao, "TRQ3DNet: A 3D quasi-recurrent and transformer based network for hyperspectral image denoising," *Remote Sens.*, vol. 14, no. 18, p. 4598, Sep. 2022.
[48] E. Korkmaz Özay and B. Tunga, "Hyperspectral image denoising with enhanced multivariance product representation," *Signal, Image Video Process.*, vol. 16, no. 4, pp. 1127–1133, Jun. 2022.
[49] B. Zhao, M. O. Ulfarsson, J. R. Sveinsson, and J. Chanussot, "Hyperspectral image denoising using spectral–spatial transform-based sparse and low-rank representations," *IEEE Trans. Geosci. Remote Sens.*, vol. 60, 2022, Art. no. 5522125.
[50] S. Xu, J. Zhang, and C. Zhang, "Hyperspectral image denoising by low-rank models with hyper-Laplacian total variation prior," *Signal Process.*, vol. 201, Dec. 2022, Art. no. 108733.

FEI MA received the B.S. degree in communication engineering and the M.S. degree in computer science from Liaoning Technical University, Fuxin, China, in 2001 and 2004, respectively, and the Ph.D. degree in circuit and system from the Beijing University of Posts and Telecommunications, Beijing, China, in 2010. He held a postdoctoral position at the University of Electronic Science and Technology of China, Chengdu, China, from 2014 to 2020. He conducted research as a Visiting Scholar with National Tsing Hua University, Hsinchu, Taiwan, from 2015 to 2016. He is currently a Faculty Member of the School of Electronic and Information Engineering, Liaoning Technical University, Huludao, China. His research interests include hyperspectral image processing, radar signal processing, pattern recognition, and convex optimization.

SIYU LIU received the B.S. degree in communication engineering from Liaoning Technical University, Huludao, China, in 2020, where she is currently pursuing the master's degree with the School of Communication and Information System. Her research interests include hyperspectral imaging denoise, deep learning, and convex optimization.

FEIXIA YANG received the B.S. and M.S. degrees in control theory and engineering from Liaoning Technical University, Fuxin, China, in 2003 and 2006, respectively, and the Ph.D. degree in circuit and system from the Beijing University of Posts and Telecommunications, Beijing, China, in 2020. She is currently a Faculty Member of the School of Electrical and Control Engineering, Liaoning Technical University, Huludao, China. Her research interests include digital image processing, remote sensing imaging, and pattern recognition.

GUANGXIAN XU received the Ph.D. degree in management science and engineering from Liaoning Technical University, Huludao, China, in 2008. Since 2013, he has been a Professor with the School of Electrical and Information Engineering, Liaoning Technical University. His research interests include digital image processing and remote sensing imaging.